Data-Driven Modeling of Wireless Power Transfer Systems With Slowly Time-Varying Parameters

Fengwei Chen, Arturo Padilla, Peter C. Young, and Hugues Garnier

***Abstract*—This article considers the data-driven modeling of a class of phase-controlled wireless power transfer (WPT) systems, where the load may vary slowly with respect to time. The dominant mode analysis suggests that a model of the Hammerstein type, which consists of a static nonlinearity function, followed by a linear time-varying model with a pure time delay, is the best structure to describe the input–output relationship of the system. On this basis, we derive a small-signal model that is linear in the variables in order to aid control design and allow the associated model parameters to be estimated from sampled input–output data using the standard refined instrumental variable (RIV) method. In the presence of a time-varying load, however, the plant model parameters may not be correctly estimated if the load response is not removed. In order to address this problem, a new recursive RIV method is proposed, in which an effective technique is introduced to track the load response, so allowing the parameters and time delay of the time-varying model to be accurately estimated. The effectiveness of the proposed method is verified by applying it to both a simulation model and a laboratory system.**

***Index Terms*—Data-driven modeling, recursive estimation, system identification, time delay, time-varying parameter, wireless power transfer (WPT).**

I. INTRODUCTION

WIRELESS power transfer (WPT) based on magnetic resonance coupling was pioneered by Tesla a century ago. The recent years have witnessed a surge of WPT in many real-world applications ranging from consumer electronics, biomedical engineering, to electric vehicles [1]–[3], especially since the time that Kurs *et al.* [4] reported their success in transferring 60 W with 40% efficiency when the distance between the sending and receiving resonators was over 2 meters. The removal of physical contact greatly improves the mobility, security, and reliability of power transfer but, at the same time, brings new challenges for effective operations of the system. One challenge can be the time-varying parameters that originate from the variation in the magnetic coupling [5] or in the load resistance [6], [7]. Such variation normally forces the output voltage/current of the system to change, even if the control variable remains constant during this process. This unexpected output fluctuation may have damaging effects on the converter or for the load. Consequently, the system should be operated with feedback control for both safety and economic reasons. To this end, an accurate model that characterizes the time-varying input–output behavior of the system would be extremely useful for control design and performance optimization.

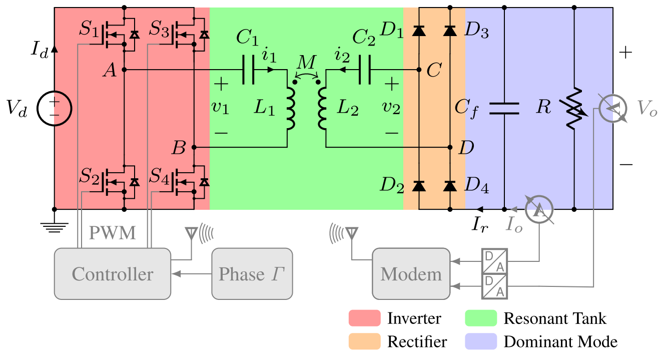

Fig. 1. WPT system with a time-varying resistive load.

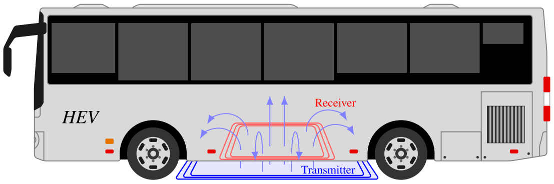

Fig. 2. Wireless charging.

This article focuses on the analysis of WPT systems with a time-varying load, as sketched in Fig. 1. Systems of this type are frequently encountered in real-life applications and one, amongst these, is the wireless charger for electric vehicles (see Fig. 2), where the battery resistance can vary with respect to time during the charging process. There are already a few papers investigating the load-independent output feature of such systems. In [8], the selection of appropriate driving frequencies to achieve maximum efficiency and load-independent

Manuscript received December 4, 2019; revised February 29, 2020; accepted April 3, 2020. Date of publication April 7, 2020; date of current version July 20, 2020. This work was supported in part by the National Natural Science Foundation of China under Grant 61703311 and in part by the China Postdoctoral Science Foundation under Grant 2017M620335. Recommended for publication by Associate Editor M. Ponce-Silva. *(Corresponding author: Fengwei Chen.)*

Fengwei Chen is with the School of Electrical Engineering and Automation, Wuhan University, Wuhan 430072, China (e-mail: fengwei.chen@whu.edu.cn).

Arturo Padilla is with the Department of Mechanical Engineering, Universidad de La Frontera, Temuco 4811230, Chile (e-mail: arturo.padilla@ufrontera.cl).

Peter C. Young is with the Systems and Control Group, Lancaster Environment Centre, Lancaster University, Lancaster LA1 4YQ, U.K. (e-mail: p.young@lancaster.ac.uk).

Hugues Garnier is with the Centre de Recherche en Automatique de Nancy, Centre National de la Recherche Scientifique, Université de Lorraine, 54000 Nancy, France (e-mail: hugues.garnier@univ-lorraine.fr).

Color versions of one or more of the figures in this article are available online at https://ieeexplore.ieee.org.

Digital Object Identifier 10.1109/TPEL.2020.2986224

voltage transfer ratio, was analyzed under the series–series and series–parallel secondary compensations. However, this paper only considered constant voltage (CV) charging and omitted consideration of constant current (CC) charging. In order to take the latter into account, a new WPT charger incorporating a reconfigurable, hybrid secondary compensation network was proposed in [9]. Both load-independent CV and CC charging can be achieved by configuration of the extra switches. More recently, a much simpler, series–series topology was proposed [7], where load-independent CV and CC outputs were achieved using an additional intermediate coil. However, all the above-mentioned methods achieve load-independent outputs via circuit topology design in the open loop. Closed-loop control has attracted little attention, perhaps due to the lack of an accurate model, especially a model that includes the time delay caused by the wireless communication link which, if it is not accounted for, would impair the feedback performance. The aim of the present paper is, therefore, to aid feedback control system design by deriving a method that is able to accurately estimate the control model parameters and time delay of a WPT system.

There are basically two groups of methods for inferring models of WPT systems: the circuit theory-based modeling method, and the data-driven modeling method [10]. The former has been well known and so cannot be over emphasized: the resulting models are physically meaningful, since they are derived from physical laws that are known to govern the system. However, the complication of the model structure, as well as the absence of time delay estimation, means that it is not the best choice for control design. Furthermore, it is worth noting that the circuit theory-based method requires *a priori* knowledge of the circuit topology and component parameters that may be difficult to acquire in practical applications. By contrast, the data-driven method adopts low-order, gray- or black-box models with time delay to describe the system; models that are very simple but can provide an accurate description of the system within the defined operating range [11]–[13]. Moreover, the related data-based mechanistic approach to modeling [12] that we utilize includes the requirement that the data-driven models should be explained in physically meaningful terms that relate to the circuit theory-based models. In such data-driven modeling, the model structure and parameters are identified, based on sampled input–output data, by minimizing the chosen performance criteria. In this regard, the data-driven method is obviously a better choice for control engineering applications, where the sampled input–output data are very easy to obtain. Such an approach has been attracting increasing attention in power electronics [6], [14]–[16].

In our previous work [10], we have addressed the problem of how to infer linear time-invariant, small-signal models for a class of series–series compensated, phase-controlled WPT systems from sampled input–output data. This article extends the research in [10] and focuses on the data-driven modeling of WPT systems with a resistive, slowly time-varying load (see also [6], [7] for related applications). A dominant mode analysis [17] is first conducted to determine the most important dynamics of the WPT system and, on this basis, we investigate how it can be modeled in the simplest manner. It is shown that a Hammerstein-type model, consisting of a static nonlinearity followed by a linear time-varying model plus a pure time delay, is the best structure because it is able to cope with the issues related to WPT, such as the nonlinearity of the inverter, time-varying loads, and time delays during power processing. Subsequently, this nonlinear model is linearized at the set point in order to obtain a linear time-varying model, which is a better form for control design. While this improves the explanatory ability of the model, the parameter estimation problem is more challenging because of the time-varying load. This not only requires the estimation of time-varying parameters, but it also makes it necessary to track and eliminate the load response caused by load variation. To this end, based on our recent work [18], a new recursive refined instrumental variable (RIV) method is proposed for continuous-time (CT) systems, in which an effective technique is introduced to track and remove the time-varying load response, so allowing the parameters and time delay of the time-varying model to be estimated accurately. The proposed recursive method can be applied in the off-line fashion when a batch of data is available, or in the on-line fashion where the model is updated every time new measurements become available.

The rest of this article is structured as follows. Section II analyzes the dominant mode of the WPT system and derives a parsimonious model to describe the most essential behavior of the system. Section III presents a method to estimate the model parameters and time delay from sampled input–output data. Sections IV and V present both numerical and real-data examples in order to demonstrate the effectiveness of the proposed method. The Appendix presents some details on the digital implementation of the filtering operation used in the proposed method. Finally, Section VI concludes this article.

II. WPT SYSTEM AND DOMINANT MODE ANALYSIS

Let us consider a single-input single-output, series–series compensated WPT system, as shown in Fig. 1. The major component of this system is a pair of loosely coupled coils L_1 and L_2, where *loosely* means that the mutual inductance M is small while the leakage inductances are large. However, the large impedance caused by the leakage inductances hinders significant power transfer through the two coils, so capacitors C_1 and C_2 are connected in series with each coil, in order to compensate for these leakage inductances. This is the so-called series–series compensation strategy, the prominent merit of which is that the choice of compensating capacitors is independent of the load [19], [20]. Therefore, by inverting the dc supply voltage V_d to an ac voltage v_1 of appropriate frequency, the resonant tank can be operated at the resonant mode, so minimizing the impedances and allowing for effective power transfer. Finally, the voltage at the receiver side, denoted as v_2, is rectified and smoothed to yield the dc output voltage V_o.

If all of the component parameters in the circuit are known, a model of the WPT system can be derived based on the circuit theory (i.e., Kirchoff's laws and dq decomposition). However, due to the numerous components in the circuit, and the mixture of ac and dc signals in analysis, the resulting model obtained by this circuit theory-based method is of quite high order, e.g., order 9, as shown in [10]. However, data-based dominant mode

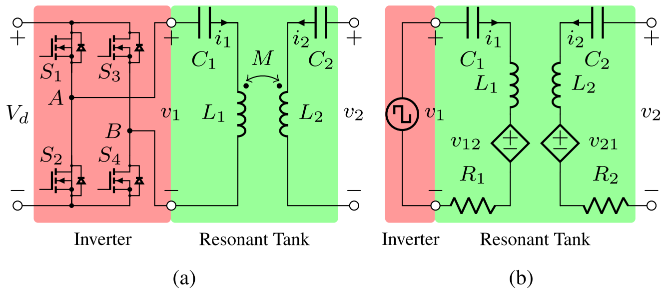

Fig. 3. Full-bridge inverter and resonant tank. $v_{12} = Mdi_2/dt$ and $v_{21} = Mdi_1/dt$ are controlled voltage sources to replace the coupling effect. (a) Circuit diagram. (b) Equivalent circuit.

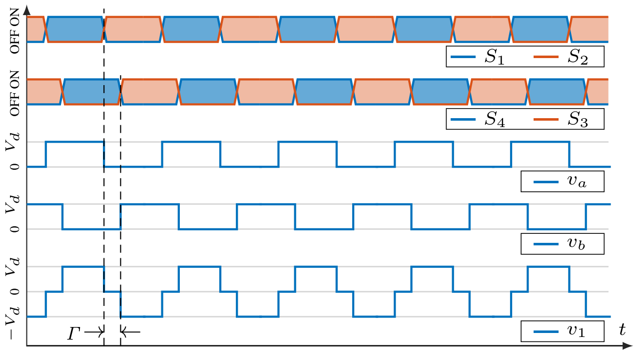

Fig. 4. Signals generated in the full-bridge inverter.

analysis [17] suggests that this model can be emulated by simpler models that are more appropriate for control system design, as discussed in Section II-E. Before this, however, we analyze the dominant physical mechanism of the WPT system from a circuit theory standpoint, and investigate how this can be modeled in the simplest manner. Note that the data shown in the later Figs. 5, 7, 9, and 10 are generated using the Simscape model presented in Section IV.

A. Inverter

A full-bridge inverter [see Fig. 3(a)] is adopted to invert the dc supply voltage V_d to a high-frequency ac voltage v_1, i.e., the difference between the output voltages of the switching legs v_a and v_b, which denote, respectively, the voltages at points A and B, in Fig. 3(a). The control variable, denoted by $\varGamma$, is the phase shift between the leading leg (S_1 and S_2) and the lagging leg (S_3 and S_4) [21]–[23]. As the inverter output v_1 is generated via pulse width modulation (PWM), which is by nature a square wave, the full-bridge inverter, together with the dc voltage source, can be replaced by a square wave voltage source if the switches are considered as ideal [see Fig. 3(b) for the equivalent circuit, and Fig. 4 for the signal waveforms generated in the inverter]. The resonant tank is highly frequency selective, allowing only the first harmonic of v_1 to pass through (see [24], [25]), so it suffices to approximate v_1 by its first harmonic, as follows:

$$\begin{aligned} v_1 &= v_a - v_b \\ &\approx \frac{2V_d}{\pi}\left[\sin\left(\omega_s t + \frac{\varGamma}{2}\right) - \sin\left(\omega_s t - \pi - \frac{\varGamma}{2}\right)\right] \\ &= \frac{4V_d}{\pi}\cos\left(\frac{\varGamma}{2}\right)\cdot\sin(\omega_s t) \end{aligned} \tag{1}$$

where ω_s is the driving frequency. Clearly, the full-bridge inverter introduces a static nonlinearity $f(\varGamma)$ in the modulation envelope of v_1

$$f(\varGamma) = \cos\left(\frac{\varGamma}{2}\right). \tag{2}$$

Note that $f(\varGamma)$ is a static function that acts instantaneously to the change of $\varGamma$ and, therefore, does not affect the low-frequency behavior of the system.

B. Resonant Tank

The resonant tank has an equivalent circuit shown in Fig. 3(b), where R_1 and R_2 are, respectively, the equivalent series resistances of the transmitter and receiver resonators, and the mutual inductance M has been replaced by two controlled voltage sources v_{12} and v_{21}. The two resonators should have the same design parameters; and they should be operated at the resonant state in order to eliminate the reactive power, as required for effective power transfer. The driving frequency of the inverter (in rad/s) is then selected as [24]

$$\omega_s = \frac{1}{\sqrt{L_1C_1}} = \frac{1}{\sqrt{L_2C_2}}. \tag{3}$$

At this frequency, the effects of the inductor and capacitor are canceled, i.e.,

$$\frac{1}{\mathrm{i}\omega_s C_j} + \mathrm{i}\omega_s L_j = 0,\ j = 1 \text{ or } 2 \tag{4}$$

where $\mathrm{i}^2 = -1$. Therefore, the resonant tank can be considered as a transformer with perfect coupling, so that the following equations are able to characterize its behavior:

$$\begin{cases} i_1R_1 + Mpi_2 = v_1 \\ Mpi_1 + i_2(R_2 + R) = 0 \end{cases} \tag{5}$$

where $p = d/dt$ is the differential operator. Once i_2 has been obtained from the solution of the above equation, the output voltage v_2 is obtained as

$$v_2 = i_2R = \frac{MRp}{M^2p^2 - R_1(R_2 + R)}v_1. \tag{6}$$

The above model can help us investigate the properties of the resonant tank. For example, when R_1 and R_2 are very small (i.e., the power losses caused by coils are negligible, which is true in a high efficiency power converter), we have

$$\lim_{R_1,R_2\to 0} v_2 = \frac{R}{Mp}v_1 \tag{7}$$

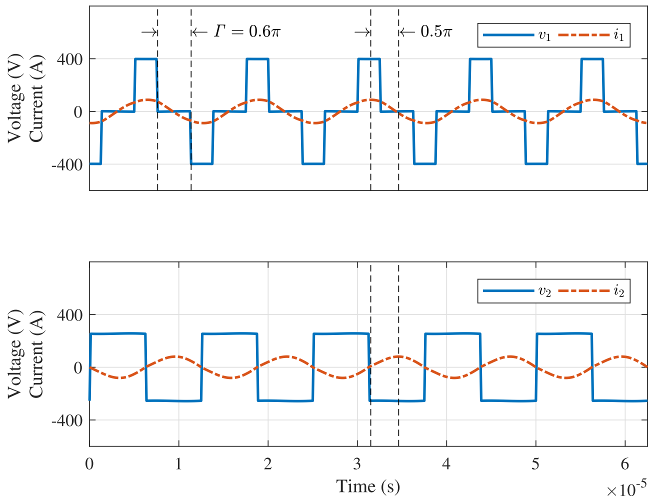

Fig. 5. Signals generated in the resonant tank using the Simscape model.

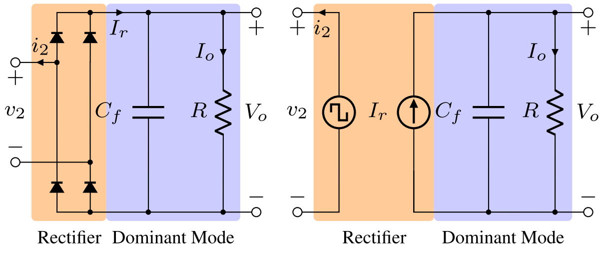

(a)

(b)

Fig. 6. Rectifier and dominant mode. (a) Circuit diagram. (b) Equivalent circuit.

showing that v_2 is an integrated version of v_1. Thus, at the limit of $R_1, R_2 \to 0$, v_2 has a 0.5π-rad phase lag compared with v_1, as evidenced in Fig. 5. Since the system is operated at a very high frequency in order to reduce the size of coupled coils, it is not hard to see that this phase lag only introduces a negligible input–output delay, so that the modulation envelope of v_2 can track the variation of Γ very quickly (see the next subsection for some numerical results).

C. Rectifier and Output Filter

The last stage of the system consists of a rectifier, required to invert the negative half-cycles of v_2 and i_2 to positive; and an output capacitor C_f, to smooth the dc output voltage V_o. Due to the absence of reactive components in the rectifier, the ac–dc conversion is completed instantaneously and does not affect the low-frequency behavior of the system. Bearing this in mind, the rectifier can be replaced by a dc current source I_r [see Fig. 6(b)].

On the other hand, a large C_f is always used to smooth the ripples in V_o. In view of this, the C_f and R in parallel constitutes the dominant mode that characterizes the low-frequency behavior of the system. Fig. 7 illustrates how C_f affects the transients of the signals generated in the circuit. When C_f is small (i.e., 10 μF), the transient behavior of V_o, as well as the modulation envelope of v_2, tracks quickly the step change of Γ: see the top and bottom panels of Fig. 7. The fast response also confirms our initial guess about the fast dynamics of the resonant tank in the previous subsection. By contrast, when the larger $C_f = 300$ μF is used, these transients slow down drastically, which validates the correctness of our dominant mode analysis: see the middle and bottom panels of Fig. 7.

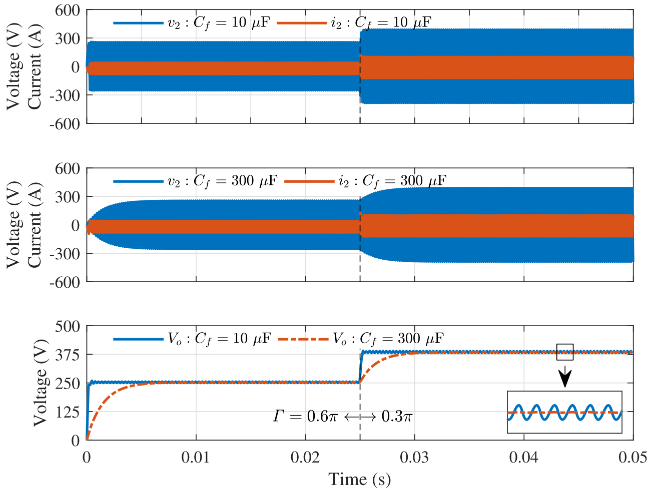

Fig. 7. Responses of a WPT system generated using the Simscape model with different output capacitances.

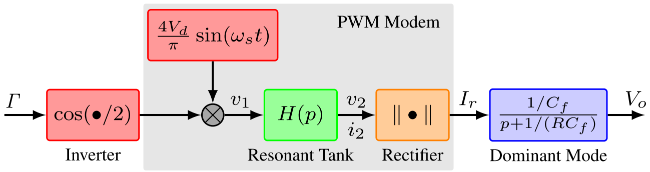

Fig. 8. Block diagram of the WPT system, where $H(p)$ is the transfer function of the resonant tank.

By simple circuit analysis, it is easy to obtain a linear transfer function that relates V_o and I_r

$$V_o = G_o(p) I_r = \frac{1/C_f}{p + 1/(C_f R)} I_r. \tag{8}$$

Furthermore, if the high-frequency circuit (i.e., the block ‘PWM Modem’ in Fig. 8) is treated as a static gain K, the relationship between V_o and Γ can be described by the following Hammerstein nonlinear model:

$$V_o = K G_o(p) f(\Gamma) \tag{9}$$

where $f(\Gamma)$ is the input nonlinearity function defined in (2). For control system design, the above nonlinear model is always linearized at the set point to yield the small-signal linear model. Let us decompose the input and output signals as follows:

$$V_o = \overline{V}_o + v_o, \ \Gamma = \overline{\Gamma} + \gamma \tag{10}$$

where the capital letters with an overline $\overline{V}_o$ and $\overline{\Gamma}$ are the static points, whereas the lowercase letters v_o and γ are the variations

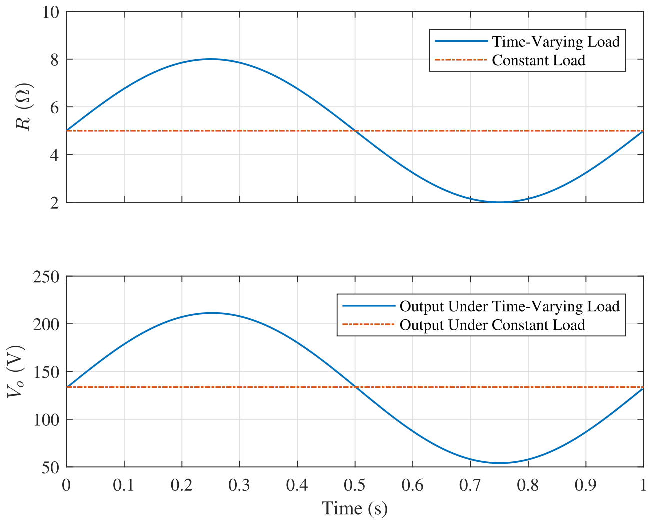

Fig. 9. Comparison of the output responses generated using the Simscape model under a constant load and a time-varying load, with $\mathit{\Gamma} = 0.8\pi$ rad. Top—Load resistance R. Bottom—Output voltage V_o.

around these static points. Then, the linearization of $f(\mathit{\Gamma})$ in (9) leads to the small-signal model

$$v_o = KG_o(p)\frac{\partial f(\mathit{\Gamma})}{\partial \mathit{\Gamma}}\bigg|_{\mathit{\Gamma}=\overline{\mathit{\Gamma}}}\gamma = -\frac{1}{2}\sin\left(\frac{\overline{\mathit{\Gamma}}}{2}\right)KG_o(p)\gamma. \tag{11}$$

D. Time-Varying Load

In general, the effects of a time-varying load are twofold: on the one hand, the output variation v_o in (11) will be the total response to the load variation r and the input variation γ; on the other hand, the parameters of the transfer function $G_o(p)$ will be time varying, due to the dependence on R, as shown in (8). As an example, Fig. 9 compares the output voltages of a system with a time-varying load and a constant load, where $\mathit{\Gamma} = 0.8\pi$ rad remains fixed in both cases. It shows that the constant load yields a constant output, while the time-varying load forces the output voltage to change, even if $\mathit{\Gamma}$ remains constant during this process. Consequently, the load variation is clearly another source of excitation and, accordingly, the small-signal model (11) should be extended to include the load variation as a new input.

Fig. 9 also shows that V_o has almost the same variation in trend as R, provided that R varies at a relatively slow rate compared with the system dynamics. In view of this, it is reasonable to model the load response variation, v_r, by a memoryless function of the load variation, r, i.e.,

$$v_r = c_0 + c_1 r + \cdots + c_{n_c} r^{n_c} \tag{12}$$

where $c_0, \ldots, c_{n_c}$ are constant coefficients and n_c is a positive integer. With this in mind, the small-signal model (11) is then extended to the following form:

$$\begin{cases} v_\gamma = G(p)\gamma \\ v_r = c_0 + c_1 r + \cdots + c_{n_c} r^{n_c} \\ v_o = v_\gamma + v_r \end{cases} \tag{13}$$

in which $G(p)$ is a linear transfer function for the plant, and v_γ is the *input response* resulting from the input variation γ. An example of the signals in (13) is shown in Fig. 10, where the bottom panel illustrates the time-varying nature of the plant model.

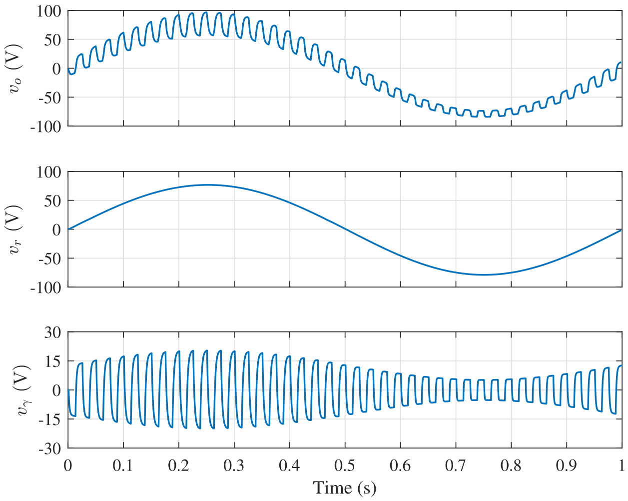

Fig. 10. Decomposition of the total response generated using the Simscape model into the input and load responses. The static points are $\overline{\mathit{\Gamma}} = 0.8\pi$ rad, $\overline{V}_o = 131.7$ V, and $\overline{R} = 5$ Ω. The input variation γ is a square wave of period 25 ms and amplitude ±0.02 rad. The load variation r (in Ω) is given by: $r = 3\sin(\pi t)$. Top—Total response v_o. Middle—Load response v_r. Bottom—Input response v_γ.

E. Model Formulation

There is still a lack of effective circuit theory-based methods to accurately determine the parameters of the conceptual model (13). To solve this problem, a simpler, data-driven approach will be developed to estimate these, based on sampled input–output data. Before this, it is assumed that the measured input is noise free

$$U(t_k) = \mathit{\Gamma}(t_k) \tag{14}$$

which holds true in control engineering applications because the control variable is generated by the controller. The noisy measurements of the output voltage V_o and current I_o data are available in the form

$$Y(t_k) = V_o(t_k) + e(t_k) \tag{15a}$$

$$Z(t_k) = I_o(t_k) + \varsigma(t_k) \tag{15b}$$

where $t_k = kT$ is the sampling instant, with T the sampling period and $k \in \mathbb{N}^+$; while $\{e(t_k)\}$ and $\{\varsigma(t_k)\}$ are two zero-mean, uncorrelated, measurement noise sequences. The load resistance is then estimated from $Y(t_k)$ and $Z(t_k)$ as

$$R(t_k) = Y(t_k)/Z(t_k). \tag{16}$$

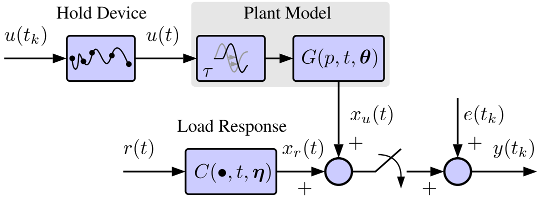

Fig. 11. Block diagram of the data-driven model (18).

Moreover, following (10) to compute the small signals $y(t_k)$, $u(t_k)$, and $r(t_k)$

$$y(t_k) = Y(t_k) - \overline{Y} \tag{17a}$$

$$u(t_k) = U(t_k) - \overline{U} \tag{17b}$$

$$r(t_k) = R(t_k) - \overline{R} \tag{17c}$$

then (13) can be reformulated in terms of the three signals (see also Fig. 11 for a block diagram of this model), i.e.,

$$\begin{cases} x_u(t) = G(p,t,\boldsymbol{\theta})u(t-\tau) = \dfrac{B(p,t,\boldsymbol{\theta})}{A(p,t,\boldsymbol{\theta})}u(t-\tau) \\ x_r(t) = C(r,t,\boldsymbol{\eta}) \\ y(t_k) = x_u(t_k) + x_r(t_k) + e(t_k) \end{cases} \tag{18}$$

in which τ is a pure time delay to account for the total time lag in the circuit; $B(p,t,\boldsymbol{\theta})$ and $A(p,t,\boldsymbol{\theta})$ are the following polynomials:

$$B(p,t,\boldsymbol{\theta}) = b_0(t)p^{n_b} + b_1(t)p^{n_b-1} + \cdots + b_{n_b}(t) \tag{19a}$$

$$A(p,t,\boldsymbol{\theta}) = p^{n_a} + a_1(t)p^{n_a-1} + \cdots + a_{n_a}(t) \tag{19b}$$

where $\boldsymbol{\theta} = [a_1(t),\ldots,a_{n_a}(t), b_0(t),\ldots,b_{n_b}(t)]^\top$ is a vector of the unknown time-varying parameters; n_a and n_b ($n_a \geqslant n_b$) are polynomial degrees; $C(r,t,\boldsymbol{\eta})$ is a polynomial defined by

$$C(r,t,\boldsymbol{\eta}) = c_0 + c_1 r(t) + \cdots + c_{n_c} r^{n_c}(t) \tag{20}$$

and $\boldsymbol{\eta} = [c_0, c_1, \ldots, c_{n_c}]^\top$ is a vector of unknown constant coefficients.

The degrees n_a and n_b are selected according to the state of the system operation: if the system is operated at the resonant state, the PWM modem in Fig. 8 can be viewed as a static gain and a first-order model is sufficient to accurately describe the system, i.e, $n_a = 1$ and $n_b = 0$, as analyzed in Section II-C. Alternatively, if the system is operated above the resonant state in order to achieve zero-voltage switchings, the resonant tank will be slightly inductive, so a higher-order model can be adopted to capture these additional dynamics. Experience shows that $n_a = 2$ and $n_b = 1$ would be enough in most situations. Another quick way to help model order selection is to check the waveform of the output response: a second-order model is suggested if an obvious oscillation exists in the output response; otherwise, a first-order model is preferred. Moreover, the selection of n_c does not seem critical provided the load is slowly time varying—a small value $n_c = 1$ or 2 will normally ensure good performance in load response tracking.

F. Objective

Let us make the following assumptions:

A1 For every time instant t, $B(p,t,\boldsymbol{\theta})$ and $A(p,t,\boldsymbol{\theta})$ have no common factors; all roots of $A(p,t,\boldsymbol{\theta})$ are located in the left-half plane;

A2 n_a, n_b, and n_c are known;

A3 The CT input $u(t)$ is generated from a discrete-time (DT) sequence $\{u(t_k)\}$ via a hold device; it is designed to be uncorrelated with $r(t)$, and is sufficiently informative to ensure the identifiability of the plant model;

A4 $r(t)$ is slowly time varying.

The objective of this paper is to recursively estimate the parameters in $\boldsymbol{\theta}$ and $\boldsymbol{\eta}$, as well as the time delay τ, from the sampled input–output data $\{y(t_\ell), u(t_\ell), r(t_\ell)\}_{\ell=1}^{k}$, where k is the number of samples, which increases by one with every recursion.

III. PROPOSED METHOD

Consider the following output error minimization problem:

$$\hat{\boldsymbol{\theta}}, \hat{\tau}, \hat{\boldsymbol{\eta}} = \arg\min_{\boldsymbol{\theta},\tau,\boldsymbol{\eta}} \frac{1}{2}\sum_{\ell=1}^{k} \varepsilon^2(t_\ell) \tag{21a}$$

$$\varepsilon(t_\ell) = y(t_\ell) - x_u(t_\ell) - x_r(t_\ell) \tag{21b}$$

where $\varepsilon(t_\ell)$ is the output error at the ℓth sampling instant. Since $u(t)$ and $r(t)$ are uncorrelated with each other (see assumption A3), the estimation error covariance between $\{\boldsymbol{\theta}, \tau\}$ and $\boldsymbol{\eta}$ is zero, so allowing an iterative, pseudo-linear regression [12] procedure for estimation, where $\{\boldsymbol{\theta}, \tau\}$ and $\boldsymbol{\eta}$ are estimated in a reciprocal manner.

A. Plant Model Parameter Estimation

For clarity of exposition, let us write $y_u(t_k) = y(t_k) - x_r(t_k)$. When $\boldsymbol{\eta}$ is tentatively known and fixed, (21b) can be written in filtered linear regression form

$$\begin{aligned} \varepsilon(t_k) &= y_u(t_k) - x_u(t_k) \\ &= y_u(t_k) - \frac{B(p,t_k,\boldsymbol{\theta})}{A(p,t_k,\boldsymbol{\theta})}u(t_k-\tau) \\ &= \frac{1}{A(p,t_k,\boldsymbol{\theta})}\left[A(p,t_k,\boldsymbol{\theta})y_u(t_k) - B(p,t_k,\boldsymbol{\theta})u(t_k-\tau)\right] \\ &= \tilde{y}_u^{(n_a)}(t_k) - \tilde{\boldsymbol{\phi}}^\top(t_k)\boldsymbol{\theta} \end{aligned} \tag{22}$$

where $(\tilde{\bullet})$ denotes the filtered version of $(\bullet)$ using the filter

$$F(p,t_k,\boldsymbol{\theta}) = \frac{1}{A(p,t_k,\boldsymbol{\theta})} \tag{23}$$

and $\tilde{\boldsymbol{\phi}}^\top(t_k)$ is the filtered regression vector

$$\tilde{\boldsymbol{\phi}}^\top(t_k) = \Big[-\tilde{y}_u^{(n_a-1)}(t_k), \ldots, -\tilde{y}_u(t_k), \tilde{u}^{(n_b)}(t_k-\tau), \ldots, \tilde{u}(t_k-\tau)\Big]. \tag{24}$$

Note that the filtering operation outlined in (23) cannot be implemented directly because $\boldsymbol{\theta}$ is not known *a priori*. Therefore, the following approximation is used in the practical implementation:

$$F(p, t_k, \boldsymbol{\theta}^*) = \frac{1}{A(p, t_k, \boldsymbol{\theta}^*)} \tag{25}$$

where, $(\bullet^*)$ denotes an initial guess of $(\bullet)$. More details of this filtering operation are presented in the Appendix.

Based on (22), the instrumental variable estimation problem is formulated as [26]

$$\begin{bmatrix} \hat{\boldsymbol{\theta}} \\ \hat{\tau} \end{bmatrix} = \arg\min_{\boldsymbol{\theta},\tau} \left\| \sum_{\ell=1}^{k} \begin{bmatrix} \hat{\tilde{\boldsymbol{\phi}}}(t_\ell) \\ \hat{\tilde{\xi}}(t_\ell) \end{bmatrix} \left[\tilde{y}_u^{(n_a)}(t_\ell) - \tilde{\boldsymbol{\phi}}^\top(t_\ell)\boldsymbol{\theta} \right] \right\|_2^2 \tag{26a}$$

$$\begin{bmatrix} \hat{\tilde{\boldsymbol{\phi}}}(t_\ell) \\ \hat{\tilde{\xi}}(t_\ell) \end{bmatrix}^\top = \left[\frac{\partial x_u(t_\ell)}{\partial \boldsymbol{\theta}}, \frac{\partial x_u(t_\ell)}{\partial \tau} \right] \Bigg|_{\boldsymbol{\theta}=\boldsymbol{\theta}^*, \tau=\tau^*} \tag{26b}$$

where $\hat{\tilde{\boldsymbol{\phi}}}(t_\ell)$ and $\hat{\tilde{\xi}}(t_\ell)$ are noise-free instruments to be used for obtaining statistically consistent estimates of $\boldsymbol{\theta}$ and τ.

1) Estimation of $\boldsymbol{\theta}$: In order to allow for time-varying parameter estimation, $\boldsymbol{\theta}(t_k)$ is modeled as a random walk process, leading to the following state-space model [12], [18]:

$$\begin{cases} \boldsymbol{\theta}(t_{k+1}) = \boldsymbol{\theta}(t_k) + \boldsymbol{w}(t_k) \\ \tilde{y}_u^{(n_a)}(t_k) = \tilde{\boldsymbol{\phi}}^\top(t_k)\boldsymbol{\theta}(t_k) + e(t_k) \end{cases} \tag{27}$$

where $\boldsymbol{w}(t_k)$ is an i.i.d., zero-mean, white noise with Gaussian amplitude distribution. Following (26b), the instrument is chosen as

$$\begin{aligned} \hat{\tilde{\boldsymbol{\phi}}}^\top(t_k) = \Big[& -\hat{\tilde{x}}_u^{(n_a-1)}(t_k), \ldots, -\hat{\tilde{x}}_u(t_k), \\ & \tilde{u}^{(n_b)}(t_k - \tau^*), \ldots, \tilde{u}(t_k - \tau^*) \Big] \end{aligned} \tag{28}$$

where $\hat{\tilde{x}}_u(t_k) = F(p, t_k, \boldsymbol{\theta}^*)G(p, t_k, \boldsymbol{\theta}^*)u(t_k - \tau^*)$. Recall that the *en bloc* RIV solution of $\boldsymbol{\theta}$ from (26a) can be written in the incremental form [27]

$$\begin{aligned} \hat{\boldsymbol{\theta}}(t_k) &= \left[\sum_{\ell=1}^{k} \hat{\tilde{\boldsymbol{\phi}}}(t_\ell)\tilde{\boldsymbol{\phi}}^\top(t_\ell) \right]^{-1} \sum_{\ell=1}^{k} \hat{\tilde{\boldsymbol{\phi}}}(t_\ell)\tilde{y}_u^{(n_a)}(t_\ell) \\ &= \boldsymbol{\theta}^* + \left[\sum_{\ell=1}^{k} \hat{\tilde{\boldsymbol{\phi}}}(t_\ell)\tilde{\boldsymbol{\phi}}^\top(t_\ell) \right]^{-1} \sum_{\ell=1}^{k} \hat{\tilde{\boldsymbol{\phi}}}(t_\ell)\varepsilon(t_\ell). \end{aligned} \tag{29}$$

Then, letting $\boldsymbol{\theta}^* \leftarrow \hat{\boldsymbol{\theta}}(t_{k-1})$ and $\tau^* \leftarrow \hat{\tau}(t_{k-1})$, the Kalman filter-based, recursive RIV implementation of (29) is summarized as (see also [18])

Prediction Step:

$$\hat{\boldsymbol{\theta}}(t_k|t_{k-1}) = \hat{\boldsymbol{\theta}}(t_{k-1}) \tag{30a}$$

$$P_{\boldsymbol{\theta}}(t_k|t_{k-1}) = P_{\boldsymbol{\theta}}(t_{k-1}) + Q_{\boldsymbol{\theta},\mathrm{nvr}} \tag{30b}$$

Correction Step:

$$\hat{\boldsymbol{\theta}}(t_k) = \hat{\boldsymbol{\theta}}(t_k|t_{k-1}) + L_{\boldsymbol{\theta}}(t_k)\varepsilon(t_k) \tag{30c}$$

$$\varepsilon(t_k) = \tilde{y}_u^{(n_a)}(t_k) - \tilde{\boldsymbol{\phi}}^\top(t_k)\hat{\boldsymbol{\theta}}(t_k|t_{k-1}) \tag{30d}$$

$$L_{\boldsymbol{\theta}}(t_k) = \frac{P_{\boldsymbol{\theta}}(t_k|t_{k-1})\hat{\tilde{\boldsymbol{\phi}}}(t_k)}{1 + \tilde{\boldsymbol{\phi}}^\top(t_k)P_{\boldsymbol{\theta}}(t_k|t_{k-1})\hat{\tilde{\boldsymbol{\phi}}}(t_k)} \tag{30e}$$

$$P_{\boldsymbol{\theta}}(t_k) = \left[I - L_{\boldsymbol{\theta}}(t_k)\tilde{\boldsymbol{\phi}}^\top(t_k) \right] P_{\boldsymbol{\theta}}(t_k|t_{k-1}). \tag{30f}$$

In the above equation, $Q_{\boldsymbol{\theta},\mathrm{nvr}}$ is a user-specified noise-variance ratio (NVR) matrix: $Q_{\boldsymbol{\theta},\mathrm{nvr}} = P_{\boldsymbol{w}}/\sigma_e^2$, where $P_{\boldsymbol{w}}$ and σ_e^2 are the covariance matrix of $\boldsymbol{w}(t_k)$ and the variance of $e(t_k)$, respectively. Also, the error covariance matrix $P_{\boldsymbol{\theta}}(t_k)$ used in the above equation is a normalized version, where σ_e^2 is removed from the expression for computational purposes but is restored for evaluation of the covariance matrix, as well as the related standard errors on the parameter estimates [12], [18]. $Q_{\boldsymbol{\theta},\mathrm{nvr}}$ allows the user to choose between the tracking ability and uncertainty: when $Q_{\boldsymbol{\theta},\mathrm{nvr}}$ is large, the algorithm can track faster the time-varying parameters, but the price to be paid is higher uncertainties on the parameter estimates; on the other hand, a small $Q_{\boldsymbol{\theta},\mathrm{nvr}}$ would be helpful to reduce the estimation uncertainties but, at the same time, it usually slows down the tracking rate.

2) Estimation of τ: Substitution of $\hat{\boldsymbol{\theta}}(t_k)$ into (22) yields

$$\breve{\varepsilon}(t_k) = \tilde{y}_u^{(n_a)}(t_k) - \tilde{\boldsymbol{\phi}}^\top(t_k)\hat{\boldsymbol{\theta}}(t_k). \tag{31}$$

Unfortunately, the nonlinear dependence between $\breve{\varepsilon}(t_k)$ and τ impedes the estimation of the time delay through a procedure that is similar to (30). Therefore, $\breve{\varepsilon}(t_k)$ should be linearized at an initial guess τ^* in order to obtain a linear-in-the-parameter formulation

$$\breve{\varepsilon}(t_k) \approx \breve{\varepsilon}(t_k, \tau^*) - \tilde{\xi}(t_k, \tau^*)(\tau - \tau^*) \tag{32}$$

where $\tilde{\xi}(t_k, \tau^*) = \tilde{\xi}(t_k)|_{\tau=\tau^*}$ and $\tilde{\xi}(t_k) = -\partial\breve{\varepsilon}(t_k)/\partial\tau$. For the derivation of $\tilde{\xi}(t_k)$, the following are the partial derivatives of the terms defined in (24), (30c)–(30e), with respect to τ:

$$\begin{aligned} \frac{\partial\tilde{\boldsymbol{\phi}}^\top(t_k)}{\partial\tau} &= \Bigg[-\frac{\partial\tilde{y}_u^{(n_a-1)}(t_k)}{\partial\tau}, \ldots, -\frac{\partial\tilde{y}_u(t_k)}{\partial\tau}, \\ &\qquad \frac{\partial\tilde{u}^{(n_b)}(t_k - \tau)}{\partial\tau}, \ldots, \frac{\partial\tilde{u}(t_k - \tau)}{\partial\tau} \Bigg] \\ &= -\Big[0, \ldots, 0, \tilde{u}^{(n_b+1)}(t_k - \tau), \ldots, \tilde{u}^{(1)}(t_k - \tau) \Big] \end{aligned} \tag{33a}$$

$$\frac{\partial\varepsilon(t_k)}{\partial\tau} = -\frac{\partial\tilde{\boldsymbol{\phi}}^\top(t_k)}{\partial\tau}\hat{\boldsymbol{\theta}}(t_k|t_{k-1}) \tag{33b}$$

$$\begin{aligned} \frac{\partial L_{\boldsymbol{\theta}}(t_k)}{\partial\tau} &= -\frac{P_{\boldsymbol{\theta}}(t_k|t_{k-1})\hat{\tilde{\boldsymbol{\phi}}}(t_k)}{\left[1 + \tilde{\boldsymbol{\phi}}^\top(t_k)P_{\boldsymbol{\theta}}(t_k|t_{k-1})\hat{\tilde{\boldsymbol{\phi}}}(t_k) \right]^2} \\ &\quad \cdot \frac{\partial\tilde{\boldsymbol{\phi}}^\top(t_k)}{\partial\tau} P_{\boldsymbol{\theta}}(t_k|t_{k-1})\hat{\tilde{\boldsymbol{\phi}}}(t_k) \\ &= -L_{\boldsymbol{\theta}}(t_k)\frac{\partial\tilde{\boldsymbol{\phi}}^\top(t_k)}{\partial\tau}L_{\boldsymbol{\theta}}(t_k) \end{aligned} \tag{33c}$$

$$\begin{aligned}\frac{\partial\hat{\boldsymbol{\theta}}(t_k)}{\partial\tau} &= \frac{\partial L_{\boldsymbol{\theta}}(t_k)}{\partial\tau}\varepsilon(t_k) + L_{\boldsymbol{\theta}}(t_k)\frac{\partial\varepsilon(t_k)}{\partial\tau}\\ &= -L_{\boldsymbol{\theta}}(t_k)\frac{\partial\tilde{\boldsymbol{\phi}}^\top(t_k)}{\partial\tau}\left[L_{\boldsymbol{\theta}}(t_k)\varepsilon(t_k) + \hat{\boldsymbol{\theta}}(t_k|t_{k-1})\right]\\ &= -L_{\boldsymbol{\theta}}(t_k)\frac{\partial\tilde{\boldsymbol{\phi}}^\top(t_k)}{\partial\tau}\hat{\boldsymbol{\theta}}(t_k). \end{aligned} \tag{33d}$$

Note that, in the derivation of the above relations, we have used the fact that the instrument $\hat{\tilde{\boldsymbol{\phi}}}(t_k)$, the filtered derivative $\tilde{y}_u^{(n_a)}(t_k)$, and all signals before t_k are independent of τ. Then, the analytical expression for $\tilde{\xi}(t_k)$ is readily obtained as

$$\begin{aligned}\tilde{\xi}(t_k) &= -\frac{\partial\breve{\varepsilon}(t_k)}{\partial\tau}\\ &= \frac{\partial\tilde{\boldsymbol{\phi}}^\top(t_k)}{\partial\tau}\hat{\boldsymbol{\theta}}(t_k) + \tilde{\boldsymbol{\phi}}^\top(t_k)\frac{\partial\hat{\boldsymbol{\theta}}(t_k)}{\partial\tau}\\ &= \left[1 - \tilde{\boldsymbol{\phi}}^\top(t_k)L_{\boldsymbol{\theta}}(t_k)\right]\frac{\partial\tilde{\boldsymbol{\phi}}^\top(t_k)}{\partial\tau}\hat{\boldsymbol{\theta}}(t_k) \end{aligned} \tag{34}$$

where the new term we need to compute is $\partial\tilde{\boldsymbol{\phi}}^\top(t_k)/\partial\tau$, while the others are available from (30). Then, following (26b) to choose the instrument

$$\hat{\tilde{\xi}}(t_k) = -pG(p, t_k, \boldsymbol{\theta}^*)u(t_k - \tau^*) \tag{35}$$

the *en bloc* solution of τ from (26a) is given by

$$\hat{\tau}(t_k) = \tau^* + \left[\sum_{\ell=1}^{k}\hat{\tilde{\xi}}(t_\ell)\tilde{\xi}(t_\ell)\right]^{-1}\sum_{\ell=1}^{k}\hat{\tilde{\xi}}(t_\ell)\breve{\varepsilon}(t_\ell). \tag{36}$$

Once again, as in (27), τ is modeled as a random walk process in order to track the parameter variation: i.e., $\tau(t_{k+1}) = \tau(t_k) + \epsilon(t_k)$, where $\epsilon(t_k)$ is white noise. Letting $\tau^* \leftarrow \hat{\tau}(t_{k-1})$, the recursive implementation of (36) is as follows:

Prediction Step:

$$\hat{\tau}(t_k|t_{k-1}) = \hat{\tau}(t_{k-1}) \tag{37a}$$

$$P_\tau(t_k|t_{k-1}) = P_\tau(t_{k-1}) + Q_{\tau,\text{nvr}} \tag{37b}$$

Correction Step:

$$\hat{\tau}(t_k) = \hat{\tau}(t_k|t_{k-1}) + L_\tau(t_k)\breve{\varepsilon}(t_k) \tag{37c}$$

$$\breve{\varepsilon}(t_k) = \tilde{y}_u^{(n_a)}(t_k) - \tilde{\boldsymbol{\phi}}^\top(t_k)\hat{\boldsymbol{\theta}}(t_k) \tag{37d}$$

$$L_\tau(t_k) = \frac{P_\tau(t_k|t_{k-1})\hat{\tilde{\xi}}(t_k)}{1 + \tilde{\xi}^\top(t_k)P_\tau(t_k|t_{k-1})\hat{\tilde{\xi}}(t_k)} \tag{37e}$$

$$P_\tau(t_k) = \left[I - L_\tau(t_k)\tilde{\xi}^\top(t_k)\right]P_\tau(t_k|t_{k-1}) \tag{37f}$$

where $Q_{\tau,\text{nvr}}$ is a scalar NVR, again to be specified by the user.

B. Load Response Estimation

Once $\hat{\boldsymbol{\theta}}(t_k)$ and $\hat{\tau}(t_k)$ have been estimated and defining $y_r(t_k) = y(t_k) - x_u(t_k)$, then (21b) can be written as

$$\varepsilon(t_k) = y_r(t_k) - x_r(t_k) = y_r(t_k) - \boldsymbol{\psi}^\top(t_k)\boldsymbol{\eta} \tag{38}$$

where $\boldsymbol{\psi}^\top(t_k) = [1, r(t_k), \ldots, r^{n_c}(t_k)]$. Since $\boldsymbol{\eta}$ is a vector of constant coefficients, it can be estimated via the conventional recursive least-squares (RLS) method

$$\hat{\boldsymbol{\eta}}(t_k) = \hat{\boldsymbol{\eta}}(t_{k-1}) + L_{\boldsymbol{\eta}}(t_k)\varepsilon(t_k) \tag{39a}$$

$$\varepsilon(t_k) = y_r(t_k) - \boldsymbol{\psi}^\top(t_k)\hat{\boldsymbol{\eta}}(t_{k-1}) \tag{39b}$$

$$L_{\boldsymbol{\eta}}(t_k) = \frac{P_{\boldsymbol{\eta}}(t_{k-1})\boldsymbol{\psi}(t_k)}{1 + \boldsymbol{\psi}^\top(t_k)P_{\boldsymbol{\eta}}(t_{k-1})\boldsymbol{\psi}(t_k)} \tag{39c}$$

$$P_{\boldsymbol{\eta}}(t_k) = \left[I - L_{\boldsymbol{\eta}}(t_k)\boldsymbol{\psi}^\top(t_k)\right]P_{\boldsymbol{\eta}}(t_{k-1}). \tag{39d}$$

Note that a theoretically more correct way to estimate the load response would be the errors-in-variables (EIV) approach [28], since both the input $r(t_k)$ and output $y_r(t_k)$ are noisy, as defined in (15). However, with the proposed RLS algorithm (39), the results have been found to be acceptable because of the low noise level in these signals and, hence, the EIV approach will not be introduced here. The interested reader should consult [28], [29] for more details.

Algorithm 1

```
Input:
    1) Sampled data: ${y(t_k), u(t_k), r(t_k)}_{k=1}^{N}$;
    2) Polynomial degrees: $n_a, n_b, n_c$;
    3) Noise variance ratios: $Q_{\boldsymbol{\theta},\text{nvr}}, Q_{\tau,\text{nvr}}$;
    4) Number of training data and number of iterations: $N_0, N_{\text{iter}}$;
Output: ${\hat{\boldsymbol{\theta}}(t_k), \hat{\tau}(t_k), \boldsymbol{\eta}(t_k)}_{k=1}^{N}$;
$y_r(t_k) \leftarrow y(t_k)$;
compute $\boldsymbol{\psi}(t_k)$ in (38);
$P_{\boldsymbol{\eta}_0} \leftarrow [\sum_{k=1}^{N_0}\boldsymbol{\psi}(t_k)\boldsymbol{\psi}^\top(t_k)]^{-1}$;
for $j \leftarrow 1$ to $N_{\text{iter}}$ do
    $\hat{\boldsymbol{\eta}}_0 \leftarrow P_{\boldsymbol{\eta}_0}\sum_{k=1}^{N_0}\boldsymbol{\psi}(t_k)y_r(t_k)$;
    compute $x_r(t_k)$ in (18);
    $y_u(t_k) \leftarrow y(t_k) - x_r(t_k)$;
    estimate ${\hat{\boldsymbol{\theta}}_0, P_{\boldsymbol{\theta}_0}}$ and ${\hat{\tau}_0, P_{\tau_0}}$ from
    ${y_u(t_k), u(t_k)}_{k=1}^{N_0}$ using an iterative identification
    method such as the one in [26];
    compute $x_u(t_k)$ in (18);
    $y_r(t_k) \leftarrow y(t_k) - x_u(t_k)$;
end
for $k \leftarrow 1$ to $N$ do
    estimate ${\hat{\boldsymbol{\theta}}(t_k), P_{\boldsymbol{\theta}}(t_k)}$, ${\hat{\tau}(t_k), P_\tau(t_k)}$, and
    ${\hat{\boldsymbol{\eta}}(t_k), P_{\boldsymbol{\eta}}(t_k)}$ using (30), (37), and (39),
    respectively;
end
```

C. Complete Algorithm

The recursive estimation method described in the previous sections requires initial parameter values, the associated estimation error covariance matrices and the NVR hyper-parameters in $Q_{\boldsymbol{\theta},\text{nvr}}$ and $Q_{\tau,\text{nvr}}$. The iterative RIV-based routines from the

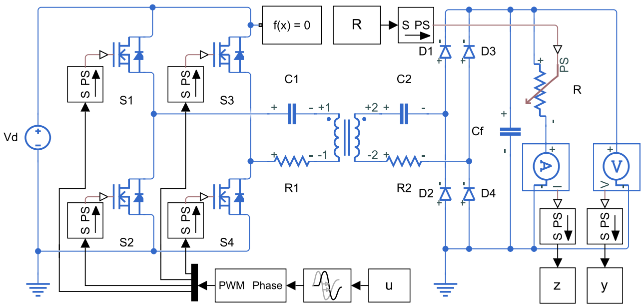

Fig. 12. Simscape diagram.

TABLE I
MAIN PARAMETERS OF THE SIMULATION DIAGRAM IN Fig. 12

Parameter	Explanation	Value
C_1	Capacitance of the sending resonator	117 nF
C_2	Capacitance of the receiving resonator	117 nF
C_f	Capacitance of the output filter	300 μF
f_s	Driving frequency of the inverter	80 kHz
L_1	Inductance of the sending resonator	34 μH
L_2	Inductance of the receiving resonator	34 μH
M	Mutual inductance between L_1 and L_2	7.33 μH
R_1	Equivalent resistance of the L_1, C_1 branch	39 mΩ
R_2	Equivalent resistance of the L_2, C_2 branch	39 mΩ
R_s	On-state resistance of the switches and diodes	12.6 mΩ
τ	Time delay	1 ms
V_d	Voltage of the dc source	400 V
V_r	Forward voltage of the diodes	0.5 V

CONTSID and CAPTAIN toolboxes[1] can be used to aid these specifications by generating initial values, based on applying these routines to a training data set; see also [26], [27]. The complete algorithm is summarized in Algorithm 1.

IV. NUMERICAL EXAMPLE

This section describes a simulation example, using a Simscape model in MATLAB, that verifies the effectiveness of the proposed method: see Fig. 12 for the Simscape diagram, and Table I for the main parameters.

A. Data Acquisition

For these simulation studies, the true time-varying load resistance (in Ω) was specified as

$$\mathring{R}(t) = 5 + 3\sin(2\pi t/1.024). \tag{40}$$

The phase $U(t)$ was redefined in the 'normalized phase' sense, which took values in [0 1], so the actual phase should be $U(t)\cdot 180^\circ$ or $U(t)\cdot\pi$ rad. In order to persistently excite the system, $U(t)$ was chosen as a pseudo-random binary sequence (PRBS) generated from a 10-stage shift register with clock period 3 ms, and its amplitude switched between 0.8 and 0.82. The input–output signals were observed for $N = 30720$ samples, at the period $T = 0.1$ ms. The measurements $Y(t_k)$ and $Z(t_k)$ were corrupted by DT white noises of variance 0.28 and 0.0001, respectively.

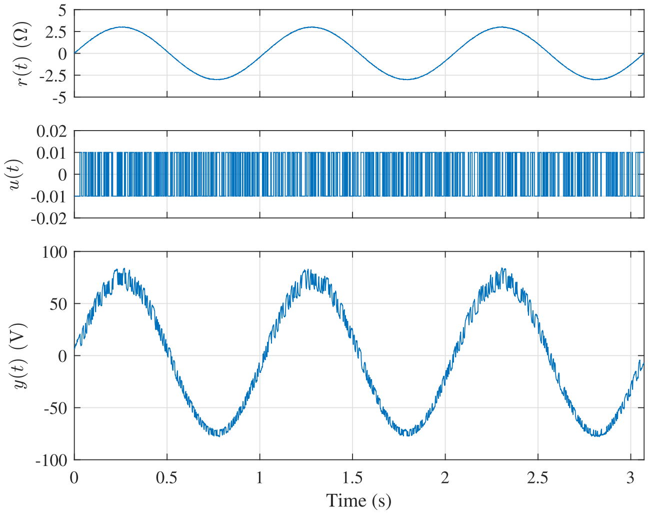

Fig. 13. Portion of simulated input–output data used for parameter estimation.

The static value for each signal was retrieved from sampled data as follows:

$$\overline{U} = \mathbb{E}\{U(t_k)\} = 0.81 \tag{41a}$$

$$\overline{Y} = \mathbb{E}\{Y(t_k)\} = 125.5 \text{ V} \tag{41b}$$

$$\overline{R} = \mathbb{E}\{R(t_k)\} = 4.999\ \Omega \tag{41c}$$

where $R(t_k) = Y(t_k)/Z(t_k)$. Then, $u(t_k)$, $y(t_k)$, and $r(t_k)$ were computed according to (17) as the perturbational dynamical data used for parameter estimation: see Fig. 13 for a snapshot of these data. As regards the inter-sample behavior, it is assumed, in this and next sections, that $u(t_k)$ is zero-order hold (ZOH), and that $y(t_k)$ is first-order hold (FOH).

B. Estimation Results

As can be seen from the bottom panel of Fig. 13, there is no obvious oscillation in the output response, even if $u(t)$ has numerous sharp steps, indicating that the system was operating at the resonant state. Then, according to the guidelines presented in the last paragraph of Section II-E, the model degrees were selected as $n_a = 1, n_b = 0$, and $n_c = 2$, leading to the following model:

$$\begin{cases} x_u(t) = G(p,t,\boldsymbol{\theta})u(t-\tau) = \dfrac{b_0(t)}{p+a_1(t)}u(t-\tau) \\ x_r(t) = C(r,t,\boldsymbol{\eta}) = c_0 + c_1 r(t) + c_2 r^2(t) \\ y(t_k) = x_u(t_k) + x_r(t_k) + e(t_k). \end{cases} \tag{42}$$

The initial parameters, as well as the error covariance matrices, were computed using the first 11 steps of Algorithm 1 based

---

[1] The CONTSID toolbox is available free through the link http://www.cran.univ-lorraine.fr/contsid/; the CAPTAIN toolbox is available free through the link http://wp.lancs.ac.uk/captaintoolbox/.

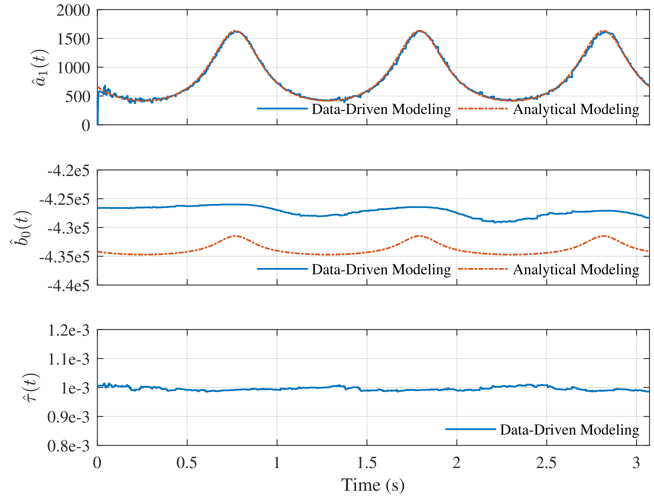

Fig. 14. Parameter estimates for the model (42) generated by the analytical method [10] and the proposed data-driven method.

on the first $N_0 = 3000$ data (the iteration number was set to $N_{\text{iter}} = 5$)

$$\tau_0 \sim \left(1.0 \cdot 10^{-3}, 6.3 \cdot 10^{-11}\right) \tag{43a}$$

$$\boldsymbol{\theta}_0 \sim \left(\begin{bmatrix} 488.0 \\ -4.3 \cdot 10^5 \end{bmatrix}, \begin{bmatrix} 9.1 \cdot 10^6 & -1.1 \cdot 10^4 \\ -1.1 \cdot 10^4 & 17.0 \end{bmatrix}\right) \tag{43b}$$

$$\boldsymbol{\eta}_0 \sim \left(\begin{bmatrix} -0.87 \\ 24.0 \\ 0.12 \end{bmatrix}, \begin{bmatrix} 4.9 & -5.7 & 1.4 \\ -5.7 & 8.7 & -2.4 \\ 1.4 & -2.4 & 0.69 \end{bmatrix} \cdot 10^{-3}\right). \tag{43c}$$

However, there is still a lack of efficient methods to determine $Q_{\boldsymbol{\theta},\text{nvr}}$ and $Q_{\tau,\text{nvr}}$ for CT models,[2] so this was achieved by trial and error, where it was found that the following values worked well:

$$Q_{\boldsymbol{\theta},\text{nvr}} = \begin{bmatrix} 200 & 0 \\ 0 & 500 \end{bmatrix}, \; Q_{\tau,\text{nvr}} = 10^{-12}. \tag{44}$$

For comparison, the analytical modeling method in [10] (a circuit theory-based method) was applied to build a small-signal model using the true parameters listed in Table I, and the load in (40). Initially, this method yielded a model of order 9, which was then reduced to first-order model using a model reduction technique (see Section IV of [10] for more details). Note that the resulting first-order model (with no time delay) has the same structure than the first equation in (42). It is computationally much more demanding to track the time-varying parameters using this approach than when using the data-based recursive estimation. This is because the computation has to be repeated at each sampling instant, leading to a total number of $N = 30720$ runs. The parameter estimates for the plant model of (42) yielded by the analytical and data-driven methods are plotted in Fig. 14, showing that the estimated $\hat{a}_1(t)$'s coincide very well while, in the case of $\hat{b}_0(t)$, they have the same variation in trend, but there is a small difference in amplitude.

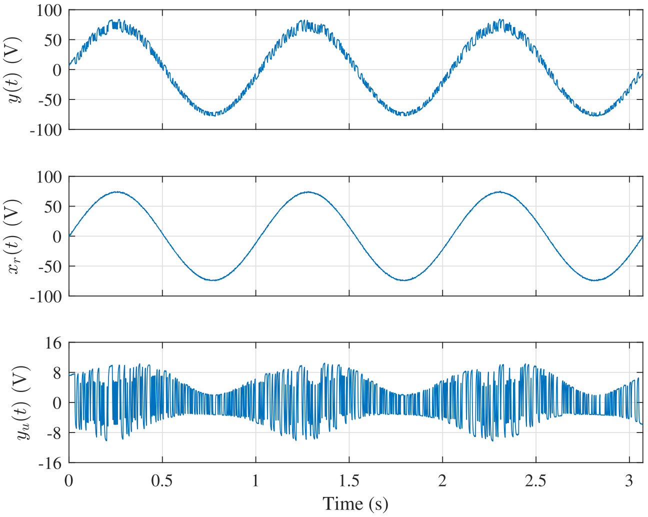

Fig. 15. Decomposition of $y(t)$ into $x_r(t)$ and $y_u(t)$. The latter two signals are defined in (45) and (46), respectively.

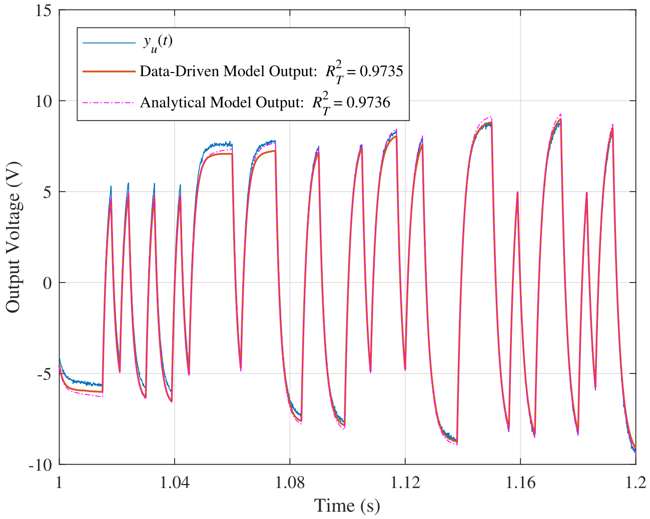

Fig. 16. Validation of the estimated model outputs using simulation data.

The load response estimated by the proposed data-driven method is given by

$$x_r(t_k) = -0.9058 + 24.59r(t_k) + 0.07823r^2(t_k) \tag{45}$$

which can be subtracted from $y(t_k)$, to yield

$$y_u(t_k) = y(t_k) - x_r(t_k). \tag{46}$$

The signals $x_r(t_k)$ and $y_u(t_k)$ obtained in this manner are shown in Fig. 15; while Fig. 16 compares the outputs of the data-driven and analytical models with $y_u(t_k)$. The models are also compared by reference to the performance index

$$R_T^2 = 1 - \frac{\|y_u(t_k) - y_s(t_k)\|_2^2}{\|y_u(t_k) - \mathbb{E}\{y_u(t_k)\}\|_2^2} \tag{47}$$

---

[2] Note that such routines, based on 'prediction error decomposition' [12] have been developed for DT models and are available in the CAPTAIN toolbox. A similar approach could be developed and used here.

TABLE II
COMPARISON OF PERFORMANCE INDEXES USING SIMULATION DATA

Method	R_T^2	Computing time
Data-driven modeling	0.9735	12.13 s
Analytical modeling	0.9736	616.2 s

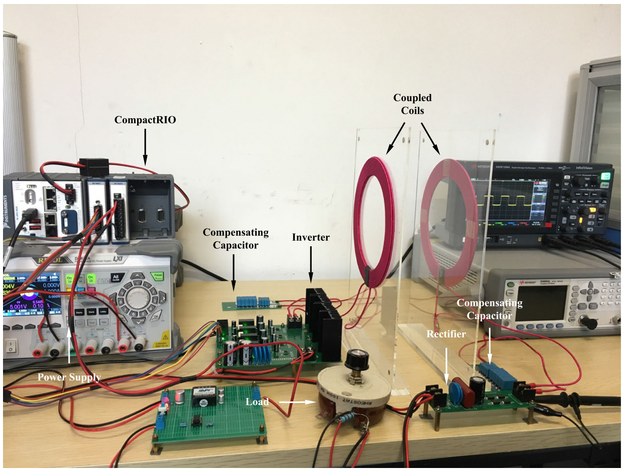

Fig. 17. Experimental apparatus.

where $y_s(t_k)$ is the simulated output of the estimated time-varying parameter model.

Note that the analytical method is not able to estimate the time delay, so the true delay $\tau = 1$ ms was used to simulate the model output. The R_T^2 ratios of the estimated models, as well as the computation times for the model estimation, are listed in Table II, showing that the two methods are identically accurate ($R_T^2 \approx 0.974$), but that the analytical method is much more time consuming (612.6 s) than the data-driven method (12.13 s). Of course, the computing time can be further reduced if C language is used for implementation (at least 50 times faster than the MATLAB language, from the authors' experience).

V. EXPERIMENTAL VALIDATION

Evaluation of the proposed method has also been based on the experimental data generated from the laboratory system shown in Fig. 17, where the measurement and control were accomplished using a National Instruments (NI) CompactRIO system consisting of an NI cRIO-9030 CPU module, an NI-9401 digital module, and an NI-9201 analog module. The two planar coils have the same design parameters (see also Fig. 18 for the geometrical shape and coil placement): they are made of Litz wire with 1200 strands to alleviate the skin effects, and the diameter of each strand is 0.01 mm; the inner diameter of the coil is 12 cm and outer diameter is 17 cm; and they are axially aligned, with the gap distance being 11 cm. The compensating capacitor bank for each coil is composed of five 6.8-nF and four 1-nF capacitors, connected in parallel. The full-bridge inverter contains four CSD19534 N-channel MOSFETs fabricated by Texas Instruments, while the rectifier is made of four SS34 Schottky diodes. In order to enhance its filtering performance, the output capacitor bank consists of three types of capacitors, including a 470-μF electrolytic capacitor, a 1-μF polypropylene capacitor, and two 100-nF ceramic capacitors. The main parameters of the transmitter and receiver resonators, as measured by a Keysight E4980AL LCR meter at 80 kHz, are shown in Table III.

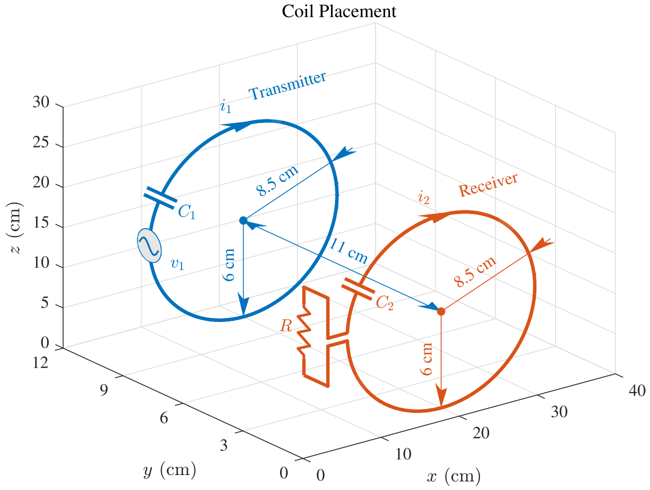

Fig. 18. Geometrical size and and placement of coupled coils.

TABLE III
MAIN PARAMETERS OF THE EXPERIMENTAL APPARATUS IN Fig. 17

Parameter	Explanation	Value
C_1	Capacitance of the sending resonator	38.59 nF
C_2	Capacitance of the receiving resonator	37.76 nF
C_f	Capacitance of the output filter	471.2 μF
f_s	Driving frequency of the inverter	80 kHz
L_1	Inductance of the sending resonator	104.4 μH
L_2	Inductance of the receiving resonator	104.3 μH
M	Mutual inductance between L_1 and L_2	8.83 μH
R_1	Equivalent resistance of the L_1, C_1 branch	161.1 mΩ
R_2	Equivalent resistance of the L_2, C_2 branch	162.4 mΩ
R_s	On-state resistance of the switches and diodes	12.6 mΩ
V_d	Voltage of the dc source	7 V
V_r	Forward voltage of the diodes	0.5 V

A. Data Acquisition

The input $U(t)$ was selected as a PRBS generated from a 9-stage shift register at a clock period of 3 ms, with its amplitude switching between 0.44 and 0.56. The load on the system was a resistor whose resistance could be adjusted by hand in the range [0 5] Ω. The phase, load voltage, and load current were observed at the time instant $t_k = kT$, where $T = 0.1$ ms and $k = 1, \ldots, 15360$. Again, the static point of each signal, estimated as the mean value of the measured data, is as follows:

$$\overline{U} = \mathbb{E}\{U(t_k)\} = 0.5 \tag{48a}$$

$$\overline{Y} = \mathbb{E}\{Y(t_k)\} = 3.263 \text{ V} \tag{48b}$$

$$\overline{R} = \mathbb{E}\{R(t_k)\} = 3.517 \, \Omega. \tag{48c}$$

The dynamical data $u(t_k)$, $y(t_k)$, and $r(t_k)$ used for model estimation were obtained according to (17), as shown in Fig. 19. It is interesting to see that the real experimental data are quite

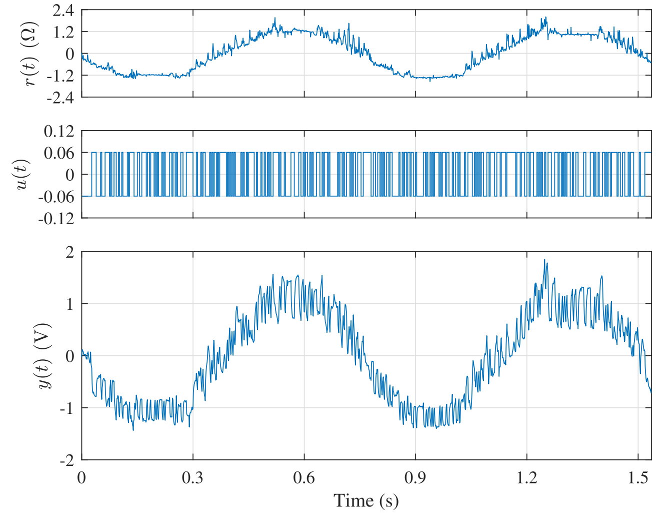

Fig. 19. Experimental data used for parameter estimation.

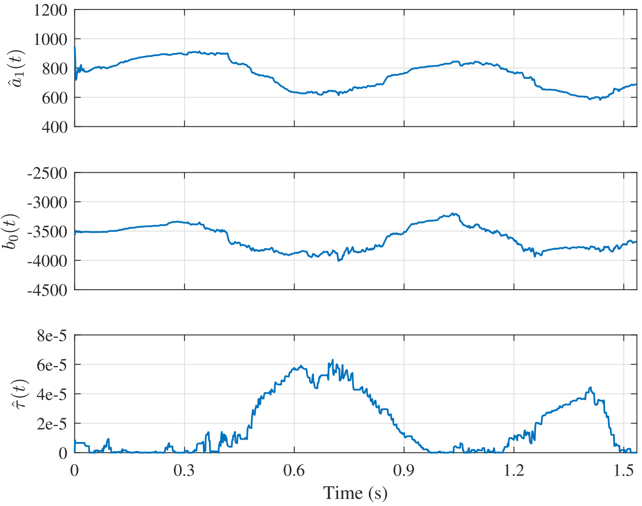

Fig. 20. Time-varying parameter estimates produced by the data-driven method.

noisy, because the MOSFETs are not ideal devices and the parasitic oscillation during the MOSFET switchings have induced these high voltage spikes. These spikes do not have zero mean value, unlike the additive noise assumed in the previous simulation example, so they will create substantial distortions in data that will naturally lead to a degradation in the accuracy in the estimated model.

B. Estimation Results

The model in equation (42) was used to describe the experimental system and this is reproduced below for convenience:

$$\begin{cases} x_u(t) = G(p,t,\boldsymbol{\theta})u(t-\tau) = \dfrac{b_0(t)}{p+a_1(t)}u(t-\tau) \\ x_r(t) = C(r,t,\boldsymbol{\eta}) = c_0 + c_1 r(t) + c_2 r^2(t) \\ y(t_k) = x_u(t_k) + x_r(t_k) + e(t_k). \end{cases} \tag{49}$$

The initial parameters τ_0, $\boldsymbol{\theta}_0$, and $\boldsymbol{\eta}_0$ and associated covariance matrices required to initiate the data-driven method, as shown below, were generated from the first $N_0 = 3000$ data points following the same procedure outlined in the previous section (i.e., use of Algorithm 1 with $N_{\text{iter}} = 5$)

$$\tau_0 \sim \left(2.0\cdot 10^{-7}, 6.3\cdot 10^{-8}\right) \tag{50a}$$

$$\boldsymbol{\theta}_0 \sim \left(\begin{bmatrix} 955.0 \\ -3.6\cdot 10^3 \end{bmatrix}, \begin{bmatrix} 1.4\cdot 10^6 & -4.1\cdot 10^5 \\ -4.1\cdot 10^5 & 1.3\cdot 10^5 \end{bmatrix}\right) \tag{50b}$$

$$\boldsymbol{\eta}_0 \sim \left(\begin{bmatrix} 0.13 \\ 1.1 \\ 0.11 \end{bmatrix}, \begin{bmatrix} 0.021 & 0.05 & 0.027 \\ 0.05 & 0.13 & 0.075 \\ 0.027 & 0.075 & 0.044 \end{bmatrix}\cdot 10^{-3}\right). \tag{50c}$$

The time-varying parameters were then estimated using the following hyper-parameters:

$$Q_{\boldsymbol{\theta},\text{nvr}} = \begin{bmatrix} 5 & 0 \\ 0 & 100 \end{bmatrix},\ Q_{\tau,\text{nvr}} = 10^{-12}. \tag{51}$$

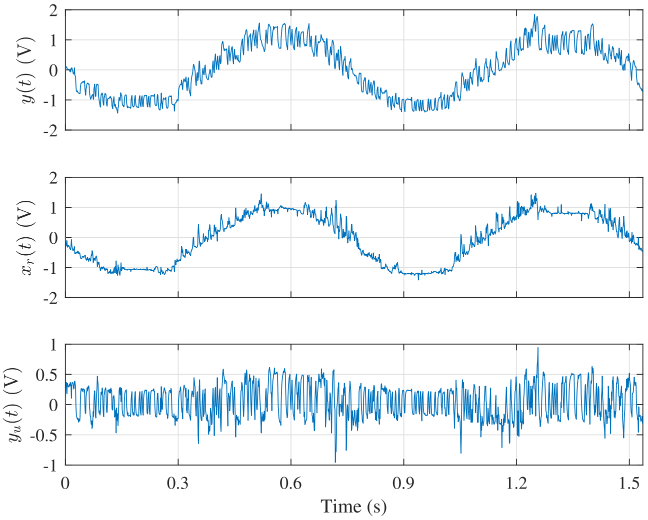

Fig. 21. Plots of $y(t)$, $x_r(t)$, and $y_u(t)$. The latter two signals are defined in (52) and (53), respectively.

The recursively estimated time-varying parameter estimates are shown in Fig. 20. The estimated time delays are quite small, because the receiver side was directly wired up to CompactRIO for data acquisition, avoiding communication delays. However, industrial applications are seldom in this fortunate situation because data are always transferred to the host computer via wireless communication, leading to much longer time delays.

The load response estimated by the data-driven method is as follows:

$$x_r(t_k) = -0.008394 + 0.8337r(t_k) - 0.04788r^2(t_k) \tag{52}$$

and, on this basis, the data for model validation was obtained as (see Fig. 21)

$$y_u(t_k) = y(t_k) - x_r(t_k). \tag{53}$$

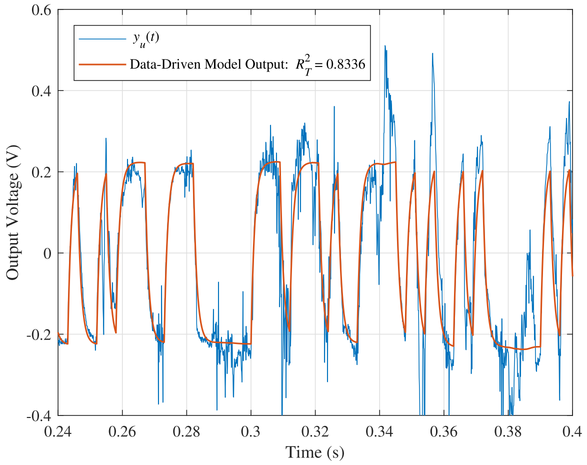

Fig. 22. Validation of the data-driven model output using experimental data.

TABLE IV
COMPARISON OF PERFORMANCE INDEXES USING EXPERIMENTAL DATA

Method	R_T^2	Computing time
Data-driven modeling	0.8336	4.336 s
Analytical modeling	0.7695	304 s

Again, the performance index, defined in (47), is computed based on $y_u(t_k)$ to evaluate the model quality; see Fig. 22 Table IV, where the time delays were set to zero for the validation of the analytical model. The results show that the data-driven method outperforms the analytical method, both in terms of the R_T^2 ratio (0.8336 vs. 0.7695) and computing time (4.336 s vs. 304 s).

Finally, based on the analysis in this and previous sections, we are able to summarize the merits of the proposed data-driven method:

- *Ease of use:* The rationale of data-driven modeling is to find a model in a specified form (here differential equations) that best describes the system. The structure and parameters of this model are identified and estimated, based on sampled data and by reference to the chosen statistical criteria. It is a standard tool that is applicable to a wide variety of modeling problems and it can be used with or without reference to the physical nature of the system. In this paper, however, we have used a 'data-based mechanistic' modeling approach (see [12]), where the physical interpretation of the model is considered essential. This has both improved the understanding of the resulting model and enhanced confidence in its efficacy when used in practical applications. In contrast to this, the conventional circuit theory-based method yields an overly complicated model for applications such as control system design; and the lack of inherent time delay estimation means that it is unable to capture the accurate delay caused by wireless communication. It also demands accurate information on the circuit topology and component parameters, which are not all that easy to obtain, especially for in-service or commercial systems. These requirements are not necessary in the application of the data-driven method and, therefore, it provides a good complement to the current circuit theory-based modeling methods.
- *Low costs:* The proposed method is a recursive estimation procedure, which needs only a few simple calculations to update the model parameters when a new observation becomes available. It is very suitable for scenarios such as real-time tracking of time-varying model parameters, due to the light computational burden in each recursion. By contrast, the analytical method, based on circuit theory, has to solve a high-dimensional, nonlinear differential equation whenever a new model is required. This is costly and not suitable for real-time implementation, especially on a micro controller, where the computing resource is limited. This is illustrated by the comparative results presented in Tables II and IV of the previous sections, which show that the computing time of the analytical method is at least 50 times larger than that of the data-driven method.

VI. CONCLUSION

This article has addressed the problem of data-driven modeling for a class of WPT systems, where the load may vary slowly with respect to time. A recursive refined instrumental variable method is proposed for estimating the parameters and time delay of a linear, time-varying parameter model of the system, as well as tracking the load response. The resulting parsimonious model, consisting of a linear time-varying model plus a pure time delay, has been shown to provide very good explanations of both simulated and experimental data. In essence, this model is able to represent well the parameter drifts during usage and time lags caused by circuit components and the communication channel. The use of the model in control design and optimization is a subject of on-going research. Other on-going research has shown that the parameter variations are probably state-dependent (see [12] and the prior references therein) and associated with inherent nonlinearity in the system dynamics caused by the load variations. An associated state-dependent parameter nonlinear model then provides a simple, constant parameter alternative to the time variable parameter model considered in the present paper.

APPENDIX
SIMULATION OF FILTERED SIGNALS

This section describes the method used for the simulation of the filtered signals from the sampled data in the presence of a time delay, as required for the digital implementation of the proposed method. Consider the following filtering operation:

$$y(t_k) = \frac{1}{A(p, t_k, \boldsymbol{\theta})} u(t_k - \tau) \tag{54}$$

where $t_k = kT$ ($k \in \mathbb{N}^+, T \in \mathbb{R}^+$) is the sampling instant, and $A(p, t_k, \boldsymbol{\theta})$ is the denominator polynomial defined in (19). The above equation can be expressed in the state-space form

$$\begin{cases} \dfrac{d\boldsymbol{x}(t_k)}{dt} = \boldsymbol{A}(t_k)\boldsymbol{x}(t_k) + \boldsymbol{B}(t_k)u(t_k - \tau) \\ y(t_k) = \boldsymbol{C}(t_k)\boldsymbol{x}(t_k) \end{cases} \tag{55}$$

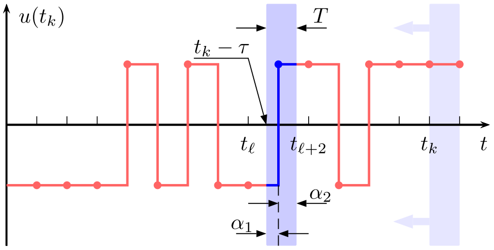

Fig. 23. Reconstruction of delayed input using ZOH (i.e., the blue line).

where

$$\boldsymbol{A}(t_k) = \begin{bmatrix} -a_1(t_k) & \cdots & \cdots & -a_{n_a}(t_k) \\ 1 & 0 & \cdots & 0 \\ & \ddots & \ddots & \vdots \\ 0 & & 1 & 0 \end{bmatrix} \tag{56a}$$

$$\boldsymbol{B}(t_k) = \begin{bmatrix} 1 & \cdots & 0 \end{bmatrix}^\top \tag{56b}$$

$$\boldsymbol{C}(t_k) = \begin{bmatrix} 0 & \cdots & 1 \end{bmatrix}. \tag{56c}$$

When τ is not an integer number of sampling periods, the delayed input is not available from the measured data set, i.e., $u(t_k-\tau) \notin \{u(t_k)\}$, so interpolation is necessary in order to recover it from the neighboring measurements. The most popular interpolation methods used in control engineering are ZOH and FOH.

With the ZOH reconstruction shown in Fig. 23, the differential equation (55) can be solved as

$$\begin{cases} \boldsymbol{x}(t_{k+1}) & = \boldsymbol{A}_d(t_k)\boldsymbol{x}(t_k) + \boldsymbol{B}_{d,1}(t_k)u(t_\ell) \\ & \quad + \boldsymbol{B}_{d,2}(t_k)u(t_{\ell+1}) \\ y(t_{k+1}) & = \boldsymbol{C}\boldsymbol{x}(t_{k+1}) \end{cases} \tag{57}$$

where ℓ is chosen such that $t_{\ell+1} \in (t_k-\tau, t_{k+1}-\tau]$, $\alpha_1 = t_{\ell+1}-(t_k-\tau)$, and $\alpha_2 = T-\alpha_1$; see Fig. 23 for a more illustrative explanation of the three terms. The sampled data model matrices take the forms

$$\boldsymbol{A}_d(t_k) = \mathrm{e}^{\boldsymbol{A}(t_k)T} \tag{58a}$$

$$\boldsymbol{B}_{d,1}(t_k) = \mathrm{e}^{\boldsymbol{A}(t_k)\alpha_2}\int_0^{\alpha_1} \mathrm{e}^{\boldsymbol{A}(t_k)\sigma} d\sigma\, \boldsymbol{B}(t_k) \tag{58b}$$

$$\boldsymbol{B}_{d,2}(t_k) = \int_0^{\alpha_2} \mathrm{e}^{\boldsymbol{A}(t_k)\sigma} d\sigma\, \boldsymbol{B}(t_k). \tag{58c}$$

In the case of FOH, an integrator is introduced with the time derivative of $u(t_k)$ as the new input (which becomes ZOH). The filtered signal can then be computed in the same manner.

REFERENCES

[1] S. Y. Hui, "Planar wireless charging technology for portable electronic products and Qi," *Proc. IEEE*, vol. 101, no. 6, pp. 1290–1301, Jun. 2013.

[2] P. Si, A. P. Hu, S. Malpas, and D. Budgett, "A frequency control method for regulating wireless power to implantable devices," *IEEE Trans. Biomed. Circuits Syst.*, vol. 2, no. 1, pp. 22–29, Mar. 2008.

[3] G. A. Covic, J. T. Boys, M. L. Kissin, and H. G. Lu, "A three-phase inductive power transfer system for roadway-powered vehicles," *IEEE Trans. Ind. Electron.*, vol. 54, no. 6, pp. 3370–3378, Dec. 2007.

[4] A. Kurs, A. Karalis, R. Moffatt, J. D. Joannopoulos, P. Fisher, and M. Soljačić, "Wireless power transfer via strongly coupled magnetic resonances," *Science*, vol. 317, no. 83, pp. 83–86, 2007.

[5] Q. Deng *et al.*, "Edge position detection of on-line charged vehicles with segmental wireless power supply," *IEEE Trans. Veh. Technol.*, vol. 66, no. 5, pp. 3610–3621, May 2017.

[6] M. Al-Greer, M. Armstrong, M. Ahmeid, and D. Giaouris, "Advances on system identification techniques for DC–DC switch mode power converter applications," *IEEE Trans. Power Electron.*, vol. 34, no. 7, pp. 6973–6990, Jul. 2019.

[7] Y. Li *et al.*, "Reconfigurable intermediate resonant circuit based WPT system with load-independent constant output current and voltage for charging battery," *IEEE Trans. Power Electron.*, vol. 34, no. 3, pp. 1988–1992, Mar. 2019.

[8] W. Zhang, S. C. Wong, C. K. Tse, and Q. Chen, "Analysis and comparison of secondary series-and parallel-compensated inductive power transfer systems operating for optimal efficiency and load-independent voltage-transfer ratio," *IEEE Trans. Power Electron.*, vol. 29, no. 6, pp. 2979–2990, Jun. 2013.

[9] R. Mai, Y. Chen, Y. Li, Y. Zhang, G. Cao, and Z. He, "Inductive power transfer for massive electric bicycles charging based on hybrid topology switching with a single inverter," *IEEE Trans. Power Electron.*, vol. 32, no. 8, pp. 5897–5906, Aug. 2017.

[10] F. Chen, H. Garnier, Q. Deng, M. K. Kazimierczuk, and X. Zhuan, "Control-oriented modeling of wireless power transfer systems with phase-shift control," *IEEE Trans. Power Electron.*, vol. 35, no. 2, pp. 2119–2134, Feb. 2020.

[11] H. Garnier and L. Wang, Eds., *Identification of Continuous-Time Models From Sampled Data*. London, U.K.: Springer-Verlag, 2008.

[12] P. C. Young, *Recursive Estimation and Time-Series Analysis: An Introduction for the Student and Practitioner*. Berlin, Germany: Springer-Verlag, 2011.

[13] H. Garnier and P. C. Young, "The advantages of directly identifying continuous-time transfer function models in practical applications," *Int. J. Control*, vol. 87, no. 7, pp. 1319–1338, 2014.

[14] T. T. Vu, S. O'Driscoll, and J. V. Ringwood, "Nonlinear dynamic transformer time-domain identification for power converter applications," *IEEE Trans. Power Electron.*, vol. 29, no. 1, pp. 318–327, Jan. 2014.

[15] V. Valdivia, A. Barrado, A. Lázaro, P. Zumel, C. Raga, and C. Fernández, "Simple modeling and identification procedures for 'black-box' behavioral modeling of power converters based on transient response analysis," *IEEE Trans. Power Electron.*, vol. 24, no. 12, pp. 2776–2790, Dec. 2009.

[16] M. Ahmeid, M. Armstrong, S. Gadoue, M. Al-Greer, and P. Missailidis, "Real-time parameter estimation of DC–DC converters using a self-tuned Kalman filter," *IEEE Trans. Power Electron.*, vol. 32, no. 7, pp. 5666–5674, Jul. 2017.

[17] P. C. Young, "Data-based mechanistic modelling, generalised sensitivity and dominant mode analysis," *Comput. Phys. Commun.*, vol. 117, pp. 113–129, 1999.

[18] A. Padilla, H. Garnier, P. C. Young, F. Chen, and J. I. Yuz, "Identification of continuous-time models with slowly time-varying parameters," *Control Eng. Pract.*, vol. 93, 2019, Art. no. 104165.

[19] Z. U. Zahid *et al.*, "Modeling and control of series–series compensated inductive power transfer system," *IEEE J. Emerg. Sel. Topics Power Electron.*, vol. 3, no. 1, pp. 111–123, Mar. 2015.

[20] Q. Deng *et al.*, "Modeling and control of inductive power transfer system supplied by multiphase phase-controlled inverter," *IEEE Trans. Power Electron.*, vol. 34, no. 9, pp. 9303–9315, Sep. 2019.

[21] M. K. Kazimierczuk, "Synthesis of phase-modulated resonant DC/AC inverters and DC/DC convertors," *IEE Proc. B—Elect. Power Appl.*, vol. 139, no. 4, pp. 387–394, Jul. 1992.

[22] D. Czarkowski and M. K. Kazimierczuk, "Phase-controlled CLL resonant converter," in *Proc. IEEE Appl. Power Electron. Conf.*, San Diego, CA, USA, Mar. 7–11, 1993, pp. 432–438.

[23] N. Kollipara, M. K. Kazimierczuk, A. Reatti, and F. Corti, "Phase-control and power optimization of LLC converter," in *Proc. IEEE Int. Symp. Circuits Syst.*, Sapporo, Japan, May 26–29, 2019, pp. 1–5.

[24] M. K. Kazimierczuk and D. Czarkowski, *Resonant Power Converters*. New York, NY, USA: IEEE Press–Wiley, 2011.

[25] A. Ayachit, F. Corti, A. Reatti, and M. K. Kazimierczuk, "Zero-voltage switching operation of transformer class-E inverter at any coupling coefficient," *IEEE Trans. Ind. Electron.*, vol. 66, no. 3, pp. 1809–1819, Mar. 2019.

[26] F. Chen, X. Zhuan, H. Garnier, and M. Gilson, "Issues in separable identification of continuous-time models with time-delay," *Automatica*, vol. 94, pp. 258–273, 2018.

[27] P. C. Young, "Refined instrumental variable estimation: Maximum likelihood optimization of a unified Box–Jenkins model," *Automatica*, vol. 51, no. 1, pp. 35–46, 2015.

[28] T. Söderström, "Errors-in-variables methods in system identification," *Automatica*, vol. 43, no. 6, pp. 939–958, 2007.

[29] S. Thil, H. Garnier, and M. Gilson, "Third-order cumulants based methods for continuous-time errors-in-variables model identification," *Automatica*, vol. 44, no. 3, pp. 647–658, 2008.

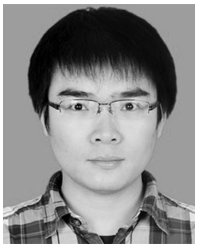

Fengwei Chen was born in Chongqing, China. He received the B.Eng. degree in automation and the M.Eng. degree in control theory and control engineering from Wuhan University, Wuhan, China, in 2009 and 2011, respectively, and the Ph.D. degree in automatic control from the Université de Lorraine, Nancy, France, in 2014.

From 2015 to 2016, he was a Lecturer with the Dalian University of Technology, Dalian, China. Since 2017, he has been with Wuhan University, where he is currently an Associate Researcher. His research interests include system identification and parameter estimation, with applications to wireless power transfer.

Arturo Padilla was born in Talcahuano, Chile. He received the D.-Ing. and the M.Sc. degrees in mechanical engineering from the Universidad de Concepción, Chile, in 2004 and 2005, respectively, and the Ph.D. degree in automatic control from the Université de Lorraine, Nancy, France, in 2017.

He is currently working at the Universidad de La Frontera, Temuco, Chile. His research interests include system identification.

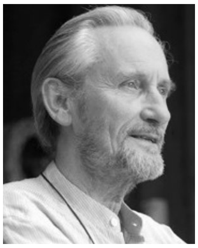

Peter C. Young received the B.Tech. and M.Sc. degrees in aeronautical engineering from Loughborough University, U.K., in 1962 and 1965, respectively, and the M.A. and Ph.D. degrees in automatic control and systems engineering from the University of Cambridge, U.K., in 1970.

From 1968 to 1970, he carried out research on self-adaptive control for the US Navy in California. In 1970, he was appointed as a Lecturer in the Engineering Department and fellow of Clare Hall, University of Cambridge. From 1975 to 1981, he was a Research Professor at the Australian National University in Canberra, Australia, where he helped to establish the Centre for Resource and Environmental Studies. From 1981 to 1987, he was the Head of the Environmental Science Department at Lancaster University, where he was instrumental in establishing the Institute of Environmental and Biological Sciences, and is currently an Emeritus Professor of Environmental Systems. In 1992, he helped to set up the Lancaster Centre for Forecasting with Prof. Robert Fildes and then directed the Centre for Research on Environmental Systems and Statistics at Lancaster. He has published over 300 papers and chapters in books; and authored or coauthored several books, including *Recursive Estimation and Time Series Analysis* (2011) and *True Digital Control* (2013). He has also been instrumental, over many years, in the development of CAPTAIN, a noncommercial MATLAB toolbox for the recursive estimation, forecasting and control of discrete and continuous-time dynamic systems. He continues to pursue research on these topics, with applications in diverse areas of research and development.

Hugues Garnier received the M.S. degree in control engineering and signal processing and the Ph.D. degree in automatic control from Université Henri Poincaré, Nancy 1, France, in 1993 and 1995, respectively.

He has been a Professor of control theory and applications with the University of Lorraine, Nancy, France, since 2003. He was a Visiting Researcher with the University of Newcastle, Australia, from 2002 to 2003, and with the University of California, San Diego, CA, USA, from 2012 to 2013. Since 2000, he has been very active in promoting direct continuous-time model-based approaches to system identification. He was the Editor of two books and was the Guest Editor for three special issues of international journals. He is also behind CONTSID, a noncommercial MATLAB toolbox for continuous-time system identification. His main research interests include system identification. His current applications include problems such as data-based modeling for battery management systems, satellite attitude control, or large flexible space structure control.